文章编号：1001-9014(XXXX)XX-0001-11

DOI:10.11972/j.issn.1001-9014.JIMW.2026138

Modeling Frequency Tuning and Radiation Power in Binary Terahertz Quantum Cascade Laser Arrays

Gao Shan-Hai[1,2], Wang Kai[1*], Tan Cheng[1,2], Gan Liang-Hua[1], Fang Yu-Long[3*], Zhang Yue-Heng[4], Xu Gang-Yi[1]

(1. National Key Laboratory of Infrared Detection Technologies, Shanghai Institute of Technical Physics, Chinese Academy of Sciences, Shanghai 200083, China;
2. University of Chinese Academy of Sciences, Beijing 100049, China;
3. Hebei Semiconductor Research Institute, Shijiazhuang 050051, China;
4. School of Physics and Astronomy, Shanghai Jiao Tong University, Shanghai 200240, China)

Abstract: Two complementary approaches are developed to model mode competition, frequency tuning, and radiation power in binary terahertz quantum cascade (THz-QCL) arrays. The first approach is based on a temporal coupled-mode theory model incorporating nonlinear gain, which efficiently simulates the evolution of the intracavity electric field amplitudes and gains after lasing onset. This approach reproduces the mode competition and frequency tuning behaviors observed in experiments, and predicts the maximum continuous tuning range of the binary THz-QCL arrays. The second approach is based on a time-domain finite-element method incorporating both nonlinear gain and gain frequency dispersion. This approach explicitly includes the detailed cavity geometry, thereby enabling accurate simulations of radiation power in addition to mode competition and frequency tuning. The simulated results are in good agreement with the experimental measurements, yielding errors of 9% in the frequency tuning range and approximately 50% in the radiation power. The combined use of these two approaches provides an effective framework for optimizing the frequency tuning range and radiation power of binary coupled laser arrays. Furthermore, these two approaches are applicable not only to binary THz-QCL arrays but can also be extended to general coupled Class-A lasers with negligible gain-response delay.

Key words: terahertz quantum cascade lasers, nonlinear gain, mode competition, frequency tuning, radiation power, temporal coupled-mode theory, time-domain finite-element method

PACS:

Introduction

Terahertz (THz) waves have important applications in material sensing, imaging, radar, wireless communications, and astrophysics[1-3]. Terahertz quantum cascade lasers (THz-QCLs) are electrically pumped semiconductor lasers based on intersubband transitions in the conduction band[4-5]. Owing to their compact size, high output power, and narrow linewidth, THz-QCLs have become one of the most important coherent radiation sources in the THz regime[6-9].

Applications such as material spectroscopy and wireless communications require THz-QCLs capable of single-mode operation and continuous frequency tunability[10-12]. Currently, the approaches for achieving continuous frequency tuning include current or temperature tuning[13], optical pumping[14], mechanical or external-cavity tuning[15-19], and coupled-cavity tuning[20-22]. Current or temperature tuning modifies the refractive index of the active region, but typically provides a limited tuning range below 5 GHz. Optical pumping enables fast tuning through carrier-induced refractive-index modulation, yet requires an external optical source and offers only limited tuning range. Mechanical and external-cavity approaches can achieve the largest continuous tuning range, reaching several hundred gigahertz, by modifying the effective refractive index, cavity length, or facet reflectivity spectrum; however, their reliance on moving components limits its long-term stability and system integration. Coupled-cavity tuning employs coupled laser arrays with independently controlled pump currents to modify the cavity refractive index, gain, or resonance frequency. Representative schemes include Vernier-effect Y-branch waveguides[20] and "π-coupled" wire lasers[22]. These ap-

Received date: 2026-05-29, 收稿日期:2026-05-29,录用日期:2026-07-13

Foundation items: Supported by the Strategic Priority Research Program of the Chinese Academy of Sciences (Nos. XDB0980000), and the National Natural Science Foundation of China (Nos. 12393833, 62435020, 62235010, and 12274285).

* **Corresponding author**: E-mail: wangkai@mail.sitp.ac.cn, yvloong@163.com

proaches offer high stability and good integrability, but the experimentally demonstrated continuous tuning range remains limited to ~20 GHz.

Recently, we proposed a new coupled-cavity electrical tuning mechanism[23]. The system consists of a binary array formed by two distributed feedback (DFB) THz-QCLs with isolated complex eigenfrequencies $\omega_i + i\alpha_i$ ($i = 1, 2$), resulting in a frequency detuning $\Delta\omega = (\omega_1 - \omega_2)/2$ and a relative loss. Due to the mutual coupling characterized by a complex coupling coefficient κ, the array supports two candidate supermodes with eigenfrequencies $\omega_\pm + i\alpha_\pm$. Our experiments demonstrated that when $\Delta\omega < |\mathrm{Im}(\kappa)|$, the competition between the two supermodes enables single-mode emission and continuous frequency tuning from approximately ω_1 to ω_2 by varying the driving currents. More importantly, the binary array can be extended to multi-element arrays for broadband frequency tuning. Experimentally, we demonstrated a coupled array containing 22 lasers and achieved continuous frequency tuning over 163 GHz.

A simplified temporal coupled-mode theory (TCMT), in which the nonlinear gain was neglected, was proposed to explain the frequency tuning in the above binary THz-QCL array[23]. Under this approximation, the temporal coupled-mode equations reduce to a non-Hermitian Hamiltonian matrix, whose eigenvalues correspond to the complex eigenfrequencies of the two supermodes. Although it can predict the supermode frequencies and tuning behavior, it suffers from several limitations. First, it neglects nonlinear gain saturation after lasing onset and therefore cannot accurately describe mode competition between supermodes. In particular, when the driving current is far above threshold, the competition between supermodes can no longer be determined solely from their modal losses. Second, the simplified model cannot describe important steady-state quantities after lasing onset, such as intracavity electromagnetic (EM) field amplitude, steady-state gain, and radiation power.

In this work, we first develop a TCMT model incorporating nonlinear gain to model frequency tuning and mode competition in binary laser arrays. Owing to its low computational cost, this approach enables rapid self-consistent calculations of steady-state lasing frequency and electric field, but cannot directly predict radiation power because it does not include the detailed cavity geometry or radiation efficiency. We further develop a time-domain finite-element method (TDFEM) incorporating both nonlinear gain and gain dispersion. Although computationally much more demanding, this method explicitly includes cavity geometry and therefore enables accurate simulations of the temporal evolution of EM field and gain, frequency tuning, and radiation power. The calculated results agree well with experiments, with errors of approximately 9% in the frequency tuning range and 50% in the radiation power.

The combined use of efficient nonlinear TCMT model and accurate TDFEM thus provides a powerful and effective framework for designing coupled-cavity laser arrays with enhanced tuning range and optimized radiation power. Moreover, the framework is applicable not only to binary THz-QCL arrays but also to general complex-coupled Class-A lasers with negligible gain-response delay, such as dye lasers and whispering-gallery-mode microcavity lasers with long photon lifetimes.

1 Experimental Results of Coupled THz-QCL Binary Arrays

The THz-QCL binary array consists of two independently pumped sub-lasers, QCL_1 and QCL_2, as schematically illustrated in Fig. 1(a). Each QCL is based on a double-metal waveguide structure consisting of metal/active-region/metal layers and contains two parts: ridge regions and common regions. The ridge regions contain six ridges forming high-index regions. Between adjacent ridges, the active region and upper metal layer are removed to form low-index regions. The periodic arrangement of high- and low-index regions constitutes a second-order DFB grating. The common regions connect ridge regions at both ends of the ridges for current injection. Since an insulating layer is inserted between the active region and the upper metal in the common regions, only the ridge regions are electrically pumped.

The second-order grating produces EM oscillations along both the grating direction and surface emission direction. Part of the EM field is injected into the neighboring sub-laser, thereby establishing mutual coupling between the two sub-lasers. In addition, the deep-subwavelength gap between the two sub-lasers further enhances the coupling strength, which is characterized by a complex coupling coefficient κ. The isolated complex eigenfrequencies of QCL_i are $\omega_i + i\alpha_i$ ($i = 1, 2$), resulting in a frequency detuning $\Delta\omega = (\omega_1 - \omega_2)/2$, and a relative loss $\Delta\alpha = (\alpha_1 - \alpha_2)/2$. Note that ω_i is the real part of the eigenfrequency and is determined by the structure of each sub-laser, while α_i refers to the loss or gain that is controllable by electric injection. Thus, $\Delta\omega$ is a fixed parameter of the array while $\Delta\alpha$ is variable.

Two groups of coupled THz-QCL arrays, denoted as Array A and B, were experimentally investigated. In Array A, the frequency detuning satisfies $\Delta\omega < |\mathrm{Im}(\kappa)|$, whereas in Array B, $\Delta\omega > |\mathrm{Im}(\kappa)|$. The purpose of these two configurations was to verify the continuity and tuning range of frequency tuning under different coupling conditions. Except for the grating period, all structural parameters are identical for all sub-lasers. Each sub-laser contains six ridges, each with a width $D = 24$ μm, a height of 10.5 μm in the z-direction, and a length of 200 μm in the y-direction The gap between the two sub-lasers is 11 μm. In Array A, the grating periods of QCL_1 and QCL_2 are $\Lambda_1 = 35$ μm and $\Lambda_2 = 37$ μm, respectively. Without gain, their isolated complex eigenfrequencies are $\omega_1 + i\alpha_1 = 3.401 + 0.014\mathrm{i}$ THz and $\omega_2 + i\alpha_2 = 3.387 + 0.013\mathrm{i}$ THz, corresponding to a frequency detuning of $\Delta\omega = 7.2$ GHz. The calculated coupling coefficient is $\kappa = 4.6 - 7.9\mathrm{i}$ GHz[23], satisfying $\Delta\omega < |\mathrm{Im}(\kappa)|$. In Array B, the grating periods are $\Lambda_1 = 35$ μm and $\Lambda_2 = 38.5$ μm. Their isolated eigenfrequencies are $\omega_1 + i\alpha_1 = 3.401 + 0.014\mathrm{i}$ THz and $\omega_2 + i\alpha_2 =$

3.376 + 0.013i THz, giving $\Delta\omega$ = 12.5 GHz. The coupling coefficient is κ = 5.2 − 9.3i GHz, satisfying $\Delta\omega > |\mathrm{Im}(\kappa)|$.

Experimentally, frequency tuning was achieved by controlling the driving currents of QCL_1 and QCL_2, denoted by $I_1$and I_2, respectively, thereby modifying the relative loss $\Delta\alpha$. To maximize the accessible range of $\Delta\alpha$, a tuning trajectory is defined as follows: the pump current of QCL_1 was first fixed at its maximum value $I_{1,\max}$, while the current of QCL_2 was gradually increased from zero to $I_{2,\max}$. Subsequently, I_2 was maintained at $I_{2,\max}$ while I_1 was gradually reduced from $I_{1,\max}$ to zero. During this process, $\Delta\alpha$ varied from its negative to positive maximum value. A current tuning parameter $d = \frac{1}{2}\left[\frac{I_{1,\max} - I_1}{I_{1,\max}} | \frac{I_2}{I_{2,\max}}\right]$ was introduced to quantitatively describe the pumping condition. The pump parameter d increases monotonically from 0 to 1 along the tuning trajectory.

The THz-QCL active region was based on a GaAs/$Al_{0.15}Ga_{0.85}As$ bound-to-continuum design, similar to that reported in Ref. [24], while the device fabrication process followed Ref. [25]. The devices operated in pulsed mode (1 μs pulse width, 10 kHz repetition) at a heatsink temperature of 20 K. The lasing spectra were measured using a Fourier-transform infrared spectrometer (Bruker 80V) with spectral resolution 2.4 GHz. The radiation power was measured using a Golay detector calibrated by a TK THz absolute power meter.

Fig. 1(c) shows the measured lasing spectra of Array A for different values of d. Throughout the tuning process, the array operated in a single-mode state, and the lasing frequency continuously shifted from 3.407 THz to 3.397 THz, corresponding to a continuous tuning range of 10 GHz. Notably, the lasing frequency did not vary strictly monotonically with d, and the minimum frequency occurred near $d \approx 0.85$. Fig. 1(d) shows the variation of radiation power with d. Along the tuning trajectory, the radiation power first increased and then decreased, reaching a maximum near $d \approx 0.5$, where both sub-lasers operated at maximum power. Power minima appeared near $d \approx 0.15$ and 0.85. Figs. 1(e) and 1(f) show the experimental results for Array B, which exhibits distinctly different tuning behavior. When $d < 0.4$, the array operated in a supermode near 3.410 THz, whose frequency redshifted with increasing d. Near d = 0.4, two lasing modes simultaneously appeared, indicating coexistence of the two supermodes $(\omega_\pm)$. When $d >$ 0.425, the lasing frequency abruptly jumped to 3.980 THz. Comparison between Figs. 1(d) and 1(f) indicates that arrays A and B exhibit similar power characteristics.

2 Modeling of Nonlinear Gain

For THz-QCL, before lasing onset, the unsaturated gain depends on the alignment of electronic subbands in the active region – which determines the population inversion and transition matrix elements – and is therefore

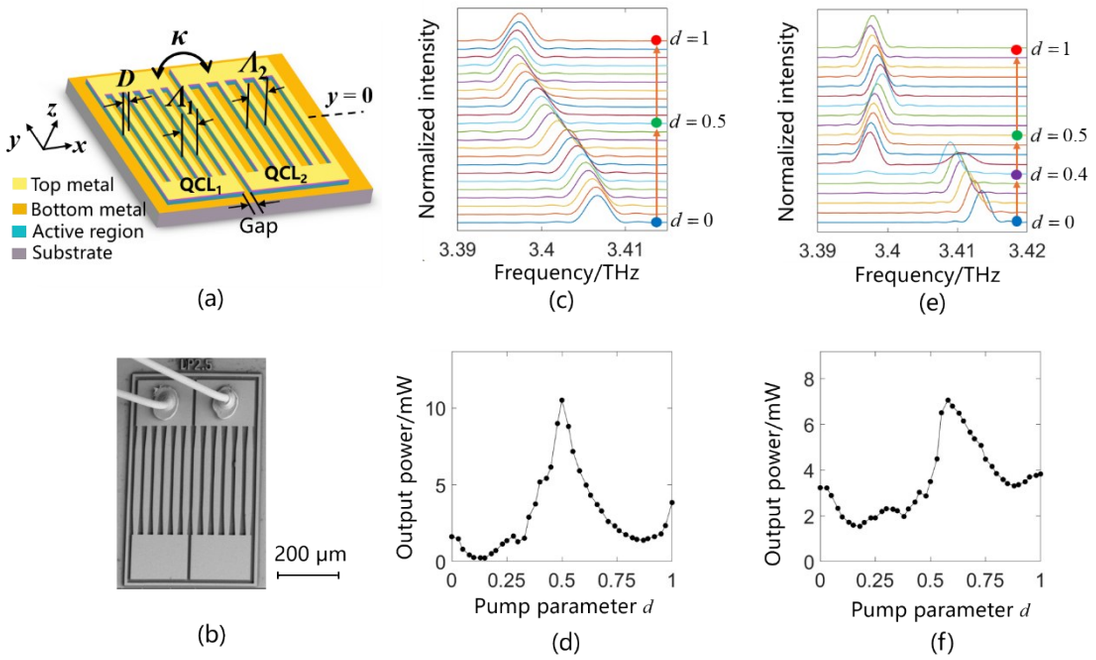

Fig. 1 Experimental results of the binary THz-QCL array: (a) Schematic of a binary THz-QCL array. The position of the y = 0 line is marked in the figure. (b) Scanning electron microscope (SEM) image of Array A. (c) Lasing spectra and (d) radiation power of Array A as the pump parameter d increases from 0 to 1. (e, f) Corresponding results for Array B. In (c) and (e), blue, purple, green, and red dots correspond to d = 0, 0.4, 0.5, and 1, respectively.

图1 二元THz-QCL阵列的实验结果:(a) 二元THz-QCL阵列的示意图,图中标出坐标系以及y = 0刻度线的位置;(b) 阵列A的扫描电子显微镜(SEM)图片;(c, d) 阵列A在泵浦参数d从0增加到1过程中的(c)激光光谱,以及(d)辐射功率;(e, f) 阵列B的对应结果。图(c)和(e)中,蓝、紫、绿和红点分别对应 d = 0、0.4、0.5和1。

a function of the bias voltage or pump current. Once the pump current exceeds threshold and lasing begins, the intracavity EM energy density rapidly increases and depletes the population inversion, resulting in gain saturation and featuring the nonlinear nature of the gain.

We first employ a Lorentz oscillator model to phenomenologically fit the effective relative permittivity $\varepsilon_r(\omega)$ of the THz-QCL active region and derive the expression for the unsaturated gain spectrum before lasing onset. The effective permittivity is expressed as

$$\varepsilon_r(\omega) = \varepsilon_\infty + \frac{f\omega_p^2}{\omega_0^2 - \omega^2 + i\omega\gamma_L}, \tag{1}$$

where ε_∞ is the high-frequency dielectric constant, ω_0 is the resonance angular frequency of the oscillator, ω_p is the plasma angular frequency, γ_L is the damping coefficient, and f is the oscillator strength associated with the population inversion and transition matrix elements. Using the definitions of complex refractive index $n = \sqrt{\varepsilon_r} = n' + in''$, together with the gain relation $g_0 = n''\omega/c$ and the assumption $n' \gg n''$, the gain spectrum can be derived from Eq. (1) as

$$g_0(\omega) = -\frac{1}{2c\sqrt{\varepsilon_\infty}} \cdot \frac{f\gamma_L\omega_p^2\omega^2}{(\omega_0^2 - \omega^2)^2 + \omega^2\gamma_L^2}, \tag{2}$$

where c is the speed of light in vacuum. The gain exhibits Lorentzian frequency dispersion. To model the nonlinear gain, the gain is assumed to be spatially uniform. Since the gain recovery time of THz-QCL active regions is typically 1 – 50 ps[26], comparable to the photon lifetime in THz-QCL cavities (~6 ps), THz-QCLs can be approximately regarded as class-A lasers[27] where the gain can instantaneously respond to changes in intracavity energy density. After lasing onset, the gain $g(\omega)$ becomes nonlinear and can be expressed as[28]

$$g(\omega) = \frac{g_0(\omega)}{1 + W/W_{sat}}, \tag{3}$$

where W is the intracavity average energy density, W_{sat} is the saturation energy density. The saturation factor is defined as $B = \frac{1}{1 + W/W_{sat}}$. Combining Eqs. (1) and (2) yields the complete nonlinear gain model for THz-QCLs:

$$g(\omega) = -\frac{1}{2c\sqrt{\varepsilon_\infty}} \cdot \frac{f\gamma_L\omega_p^2\omega^2}{(\omega_0^2 - \omega^2)^2 + \omega^2\gamma_L^2} \frac{1}{1 + W/W_{sat}}. \tag{4}$$

Experimental measurements show that the gain spectrum of the active region used in this work is centered at 3.4 THz with a full width at half maximum of 0.3 THz. The real part of the effective refractive index is 3.55. Near the lasing frequency $\omega = \omega_0$, the waveguide loss, primarily caused by free-carrier absorption and absorption in the metal layers, is approximately 10 cm^{-1} and is assumed to be independent of the driving current. As the driving current increases from zero to the resonance alignment condition, the active-region gain increases from 0 to approximately 50 cm^{-1}. Accordingly, the active-region net gain varies from −10 to 40 cm^{-1}, corresponding to a gain rate G_0 varying from −12 to 50 GHz. Our previous work[29] showed that the saturation energy density is approximately W_{sat} = 0.08 J/m^3. Under these conditions, the fitting parameters are obtained as ω_0 = 3.4 THz, γ_L = 0.3 THz, ω_p = 0.72 THz, and ε_∞ = 12.6. The oscillator strength f varies from 0.2 to −0.8 depending on the injection current.

In the TCMT model, the directly calculated quantity is the complex electric field amplitude $a(t)$, while the intracavity energy density is proportional to the squared magnitude of $a(t)$, i. e., $W \propto |a|^2$. Therefore, the saturation factor can also be expressed as B=11+|a|2/|asat|2, where a_{sat} = 7.9×10^4 V/m is the saturation electric field amplitude.

3 Simulations Based on Nonlinear Temporal Coupled-Mode Theory Model

We now employ the nonlinear TCMT[30-32] model to investigate the frequency tuning characteristics and intracavity energy density of binary THz-QCL arrays. To simplify the calculations, gain dispersion is neglected in this section. The temporal evolution of the complex electric field amplitudes $a_1(t)$ and $a_2(t)$ in QCL_1 and QCL_2, respectively, can be described by[33]

$$da1dt = i\omega 1 - \alpha 1 + G0,11 + |a1|2/|asat|2a1 + i\kappa a2, \tag{5a}$$

$$da2dt = i\omega 2 - \alpha 2 + G0,21 + |a2|2/|asat|2a2 + i\kappa a1, \tag{5b}$$

where $\omega_{1,2}$ and $\alpha_{1,2}$ are the real eigenfrequencies and loss rates of the isolated cavities, respectively, and are independent of pumping conditions. $G_{0,1}$and $G_{0,2}$ are the unsaturated gain rates of the QCL_1 and QCL_2, respectively, and are associated with the pump currents. For simplicity, we assume that the coupling coefficient κ does not vary with pump current, and its value has been given in Section 1. During operation, the only tunable parameters are the pump currents, corresponding to $G_{0,1}$ and $G_{0,2}$. The intracavity electric fields E_1 and E_2 in QCL_1 and QCL_2 are defined as the real parts of a_1 and a_2, respectively, i. e., $E_1 = \mathrm{Re}[a_1]$ and $E_2 = \mathrm{Re}[a_2]$. By numerically solving Eq. (5), we simulate the dynamics of the system under different $G_{0,1}$ and $G_{0,2}$ conditions. The initial values of $a_{1,2}(t)$ are chosen to be close to zero, which does not affect the steady-state solutions.

We first consider the special case where $G_{0,1}$ = $G_{0,2}$ = 50 GHz, corresponding to both sub-lasers operate at maximum pump current and a pump parameter d = 0.5. For Array A, Fig. 2 shows the calculated temporal evolution of E_1 and E_2, their corresponding steady-state spectra obtained by Fourier transform, and the gain evolution. Figs. 2(a) – 2(c) show that after approximately 200 ps, E_1 and E_2 evolve into harmonic oscillations with constant amplitude and a common oscillation frequency of 3.3988 THz. This indicates that the two sub-lasers maintain a constant phase difference, confirming the synchronization between them. Fig. 2(d) shows the gain evolution in the two sub-lasers, illustrating that as lasing builds up and the field amplitude increases, the gains rapidly decrease and eventually stabilize at different steady-state values of 6.3 GHz and 8.9 GHz. Notably, the frequency-domain eigenmode analysis predicts two supermodes with eigenfrequencies 3.389 − 0.033i THz

and 3.402−0.043i THz, both exceed threshold. However, frequency-domain analysis alone cannot determine the outcome of mode competition or calculate the steady-state field amplitudes and gains. In contrast, the time-domain calculations directly reveal the temporal evolution of the intracavity fields and gains, as well as the final outcome of mode competition.

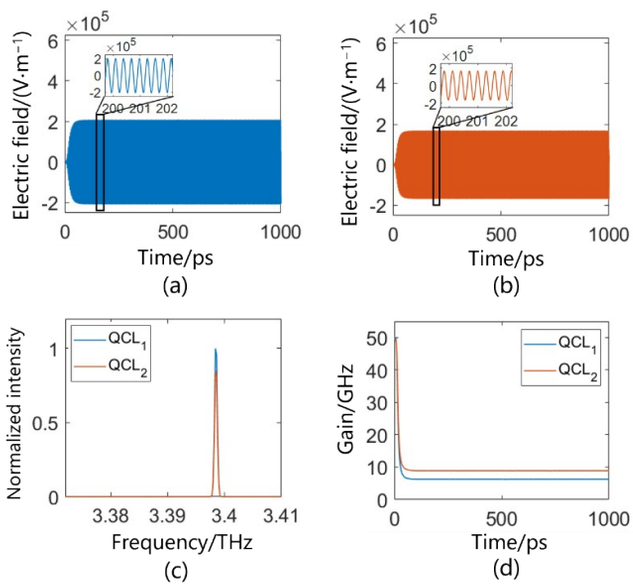

Fig. 2 Simulations of the lasing dynamics of Array A based on the nonlinear TCMT model under the condition $G_{0,1} = G_{0,2}$ =50 GHz: (a, b) Temporal evolution of E_1 and E_2, respectively, with enlarged views shown in the insets. (c) Steady-state spectra of E_1 and E_2. (d) Temporal evolution of the gain rates. In all panels, the blue and red curves are associated with QCL_1 and QCL_2, respectively.
图 2 在 G0,1=G0,2= 50 GHz 的条件下,阵列 A 基于非线性 TCMT 模型的激射过程的模拟:(a, b) 分别为 E1 和 E2 的时域演化,插图为局部放大图;(c) E1 和 E2 的稳态频谱;(d) 增益速率的时域演化。在所有图中,蓝色和红色曲线分别对应 QCL1 和 QCL2 有关的物理量。

Fig. 3 presents the corresponding results for Array B. In this case, E_1 and E_2 exhibit periodic oscillations. Fourier-transform analysis (Fig. 3(c)) shows that the array simultaneously supports two lasing modes at 3.383 and 3.398 THz, which indicates that the two sub-lasers are not synchronized. Compared with the experimental results in Fig. 1(e), dual-mode lasing was observed at slightly different value of d (d = 0.4) with frequencies 3.397 and 3.409 THz, consistent with the simulations. Note that E_1 and E_2 oscillate at the beat frequency between the modes, and the gains also exhibit oscillations at the same frequency.

We further investigate the lasing frequency and average intracavity energy density of the two sub-lasers under different values of $G_{0,1}$and $G_{0,2}$. Since the directly tunable quantities in the TCMT model are the unsaturated gain rates rather than the driving currents, we define a gain tuning trajectory analogous to the experimental procedure. The gain parameter is defined as $d' = \frac{1}{2}\left(\frac{G_{0,\max} - G_{0,1}}{G_{0,\max} - G_{0,\min}} | \frac{G_{0,2} - G_{0,\min}}{G_{0,\max} - G_{0,\min}}\right)$, which monotonically increases from 0 to 1. Since the unsaturated gain is not linearly related to the pump current in THz-QCLs[34], the current tuning parameter d and gain tuning parameter d' are not strictly equivalent. The average intracavity energy density is defined as $W_{ave} = (W_1 + W_2)/2$, where W_1 and W_2 are the intracavity energy densities of QCL_1 and QCL_2, respectively. As discussed in Section 2, W_1 and W_2 are proportional to $|a_1|^2$ and $|a_2|^2$, respectively. Since the radiation power is proportional to W_{ave}, W_{ave} provides a qualitative estimate of the radiation power.

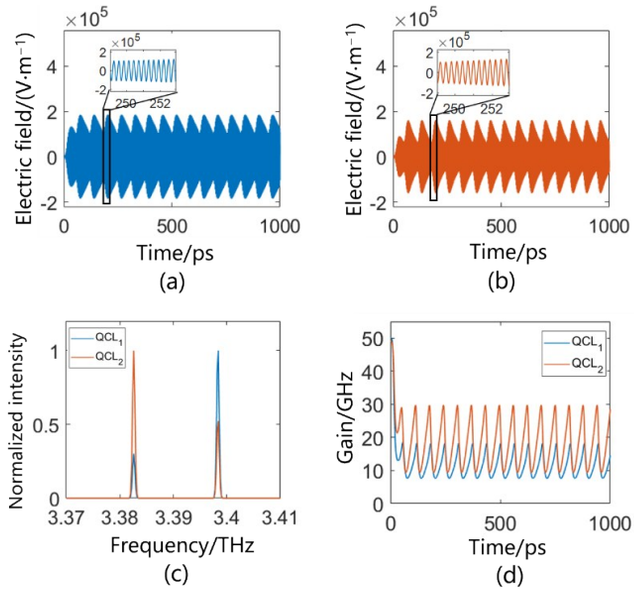

Fig. 3 Simulations of the lasing dynamics of Array B based on the nonlinear TCMT model under the condition $G_{0,1} = G_{0,2}$ =50 GHz: (a, b) Temporal evolution of E_1 and E_2, respectively, with enlarged views shown in the insets. (c) Steady-state spectra of E_1 and E_2. (d) Temporal evolution of the intracavity gain rates. In all panels, the blue and red curves are associated with QCL_1 and QCL_2, respectively.
图 2 在 G0,1=G0,2= 50 GHz 的条件下,阵列 B 基于非线性 TCMT 模型的激射过程的模拟:(a, b) 分别为 E1 和 E2 的时域演化,插图为局部放大;(c) E1 和 E2 的稳态频谱;(d) 增益速率的时域演化。在所有图中,蓝色和红色曲线分别对应 QCL1 和 QCL2 有关的物理量。

For Array A, the two sub-lasers remain synchronized throughout the entire tuning process, and consequently, the array maintains single-mode operation. The calculated steady-state spectra of the intracavity electric fields and W_{ave} (normalized to the value at d' = 0.5) are shown in Figs. 4(a) and 4(b). As d' increases from 0 to 1, the lasing frequency continuously redshifts from 3.4021 THz to 3.3904 THz, corresponding to a tuning range of 11.7 GHz, in good agreement with the experimentally measured 10 GHz tuning range. W_{ave} exhibits a trend similar to the experimentally measured radiation power shown in Fig. 1(d).

For Array B, Figs. 4(c) and 4(d) show the steady-state spectra of E_1 and normalized W_{ave}. When $0 < d' < 0.45$, the two sub-lasers are synchronized. The array op-

erates near 3.400 THz and redshifts with increasing d'. When $0.5 < d' < 0.7$, two modes coexist near 3.382 and 3.399 THz, and the two sub-lasers are not synchronized. When $0.7 < d' < 1$, the lasing frequency abruptly switches to 3.380 THz, and the two sub-lasers are synchronized again. The tuning process is therefore discontinuous and involves dual-mode coexistence and frequency switching, consistent with the experimental observations in Fig. 1(e). The quantitative discrepancy mainly arises because the tuning parameter d is not linearly related to the gain tuning parameter d'. W_{ave} calculated for Array B differs noticeably from the experimentally measured power trend. Besides the nonlinear relationship between d and d', another important reason may be that different lasing modes possess different radiation efficiencies.

These results demonstrate that frequency-domain eigenvalue analysis can only predict candidate supermodes and determine whether they are above the lasing threshold, but cannot describe mode competition or gain saturation after lasing onset. In contrast, the nonlinear TCMT model directly predicts the mode competition, and frequency-tuning behavior of coupled laser arrays, as well as important steady-state quantities such as gain and intracavity energy density.

In the following, we scan the detuning and relative net loss $\Delta\alpha = [\alpha_1 - G_{0,1} - (\alpha_2 - G_{0,2})]/2$ of the two sub-lasers to predict the maximum tuning range. Fig. 5(a) shows the distribution of the lasing frequency ω_{lasing} in the parameter space $(\Delta\omega, \Delta\alpha)$. Since the eigenfrequencies of the resonators and the corresponding detuning $\Delta\omega$ are intrinsic properties of the resonators and do not vary with the pump current, the tuning trajectory appears as horizontal straight lines. As $\Delta\omega$ increases from zero, continuous tuning occurs first, and the tuning range expands (as shown in Fig. 5(b)). However, when $\Delta\omega > |\mathrm{Im}(\kappa)|$, discontinuous tuning occurs. The maximum continuous tuning range is found to be 13.5 GHz. Overall, the results are similar to those obtained with the linear gain model[23]. The qualitative difference is that the nonlinear gain model can accurately predict the asynchronous region (the brown region in Fig. 5(a)).

4 Simulations Based on Nonlinear Time-Domain Finite-Element Method

We now combine the nonlinear gain and gain dispersion model developed in Section 2 with a TDFEM (implemented using the transient EM-wave module in COMSOL Multiphysics) to systematically investigate mode competition, frequency tuning, and radiation characteristics of the coupled binary laser arrays. Using Eq. (1), the frequency-domain polarization $P(\omega) = \varepsilon_0[\varepsilon_r(\omega) - \varepsilon_\infty]E(\omega)$ can be transformed into the time domain through inverse Fourier transformation, yielding a differential equation for the polarization. The resulting equation used in the TDFEM simulations is given by [35]

$$\frac{\partial^2 P(t)}{\partial t^2} + \gamma_L \frac{\partial P(t)}{\partial t} + \omega_0 P(t) = \varepsilon_0 \omega_p^2 \frac{f}{1 + W/W_{sat}} E(t). \quad (6)$$

Applying this equation to the THz-QCL active region enables frequency-dispersive saturated gain. It should be noted that, although gain dispersion is includ-

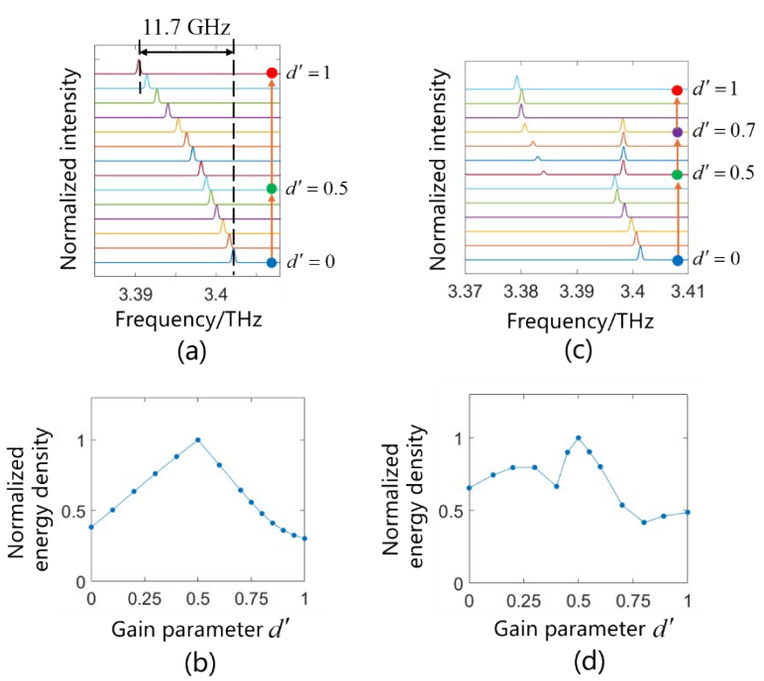

Fig. 4 Simulated tuning characteristics of representative binary THz-QCL arrays based on the nonlinear TCMT model: (a) Lasing spectra and (b) normalized W_{ave} of Array A as the gain parameter d' increases from 0 to 1. (c, d) Corresponding results for Array B. In (a) and (c), blue, green, purple, and red dots correspond to $d' = 0$, 0.5, 0.7 and 1, respectively.

图4 基于非线性TCMT模型的典型二元THz-QCL阵列调谐特性的模拟结果:(a, b)阵列A在增益参数d'从0增加到1过程中的(a)激射光谱,以及(b)归一化的Wave;(c, d)阵列B对应的结果。图(a)和(c)中,蓝、绿、紫和红点分别对应d'= 0、0.5、0.7和1。

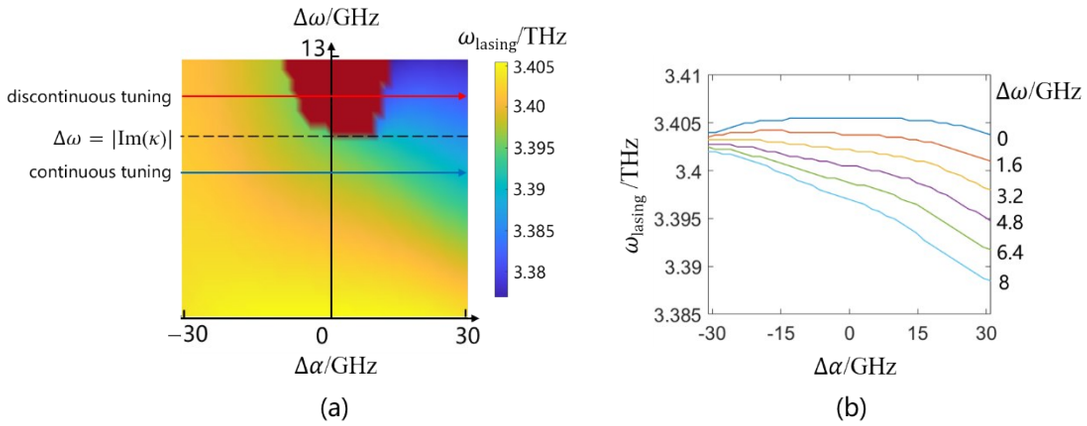

Fig. 5 Simulation results based on the nonlinear TCMT model with κ = 4. 5 + 9. 3i GHz: (a) Distribution of the lasing frequency ω_{lasing} in the parameter space ($\Delta\omega$, $\Delta\alpha$). Continuous tuning occurs when $\Delta\omega < |\mathrm{Im}(\kappa)|$, and discontinuous tuning occurs when $\Delta\omega > |\mathrm{Im}(\kappa)|$. The brown region in the figure indicates the asynchronous state of multimode oscillation, where no single lasing frequency exists. (b) Variation of ω_{lasing} along the continuous tuning trajectory for different values of $\Delta\omega$.
图 5 二元 THz-QCL 阵列基于非线性 TCMT 模型(其中 κ = 4. 5 + 9. 3i GHz)的模拟结果:(a) 激射频率 ωlasing 在参数空间(Δω, Δα)中的分布。当 Δω < |Im(κ)|时发生连续调谐,当 Δω > |Im(κ)|时发生非连续调谐。图中棕色区域表示多模振荡的非同步态,在该区域内不存在单一的激射频率。(b) 对于不同的 Δω 值,ωlasing 沿连续调谐路径的变化。

ed in the TDFEM, its effect on the calculated lasing frequencies is negligible, because the lasing frequency range (3. 38 − 3. 40 THz) is centered at the peak of the gain spectrum and the gain varies only slightly (<0. 2%) over this frequency range. Nevertheless, gain dispersion should still be incorporated into the TDFEM, since a nondispersive gain medium may cause the electromagnetic fields to diverge during the time-domain finite-element simulations.

Because full three-dimensional (3D) time-domain finite-element simulations are computationally intensive, the following simplification is adopted. Based on previous experimental observations[23], the EM field exhibits a fundamental transverse mode along the *y*-direction. Therefore, the device can be approximated as infinitely extended along the *y*-direction with invariant field distribution, reducing the 3D problem to a two-dimensional (2D) simulation in the *x*–*z* plane, as illustrated in Fig. 6. Based on our experience with eigenfrequency simulations, the eigenfrequency discrepancy introduced by this approximation is generally less than 1%. During the simulations, electric dipole sources are placed at the center of each ridge (as indicated by the red dots in Fig. 6) to mimic spontaneous emission. All dipoles have identical dipole moments polarized along the *z*-direction, with the expression $p(t) = p_0 \exp[-(t-t_0)^2/2\sigma^2]\sin[\omega_0(t-t_0)]$, where $p_0 = 3\times10^{-4}$ A·m, $t_0 = 35$ ps, $\omega_0 = 3.4$ THz, and $\sigma = 5$ ps. Probes are placed inside the cavities of QCL_1 and QCL_2 (as indicated by the black crosses in Fig. 6) to monitor the temporal evolution of the *z*-component electric fields $E_{z,1}$ and $E_{z,2}$.

As in Section 3, we first consider the case $G_{0,1} = G_{0,2} = 50$ GHz. Fig. 7 shows the simulation results of Array A. Figs. 7(a) and 7(b) show the temporal evolution of $E_{z,1}$ and $E_{z,2}$, illustrating that, after roughly 680 oscillation cycles, both fields reach a steady state with constant amplitudes. Fig. 7(c) presents the normalized steady-state spectrum, showing single-mode lasing at 3. 398 THz, which confirms synchronization between them. Fig. 7(d) shows the temporal evolution of gains in the two sub-lasers. As lasing builds up and the intracavity energy density increases, the gains rapidly decrease and eventually stabilize at 5. 3 GHz and 9. 5 GHz.

Fig. 8 presents the corresponding results for Array B. In this case, the array simultaneously supports two lasing modes at 3. 380 and 3. 397 THz, and the two sub-lasers are asynchronized. QCL_1 predominantly supports the 3. 397 THz mode, which is reflected by the nearly

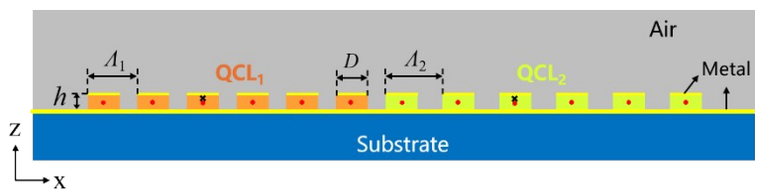

Fig. 6 Cross-sectional schematic of the binary THz-QCL array. The orange and yellow-green regions represent the active regions of QCL_1 and QCL_2, respectively. The red dots within the active regions denote electric dipole excitation sources, and the black crosses indicate field probes.
图 6 二元 THz-QCL 阵列的横截面示意图。其中橙色和黄绿色分别代表 QCL1 和 QCL2 的有源区,有源区内红色点代表电偶极子激励源,黑色叉代表场探针。

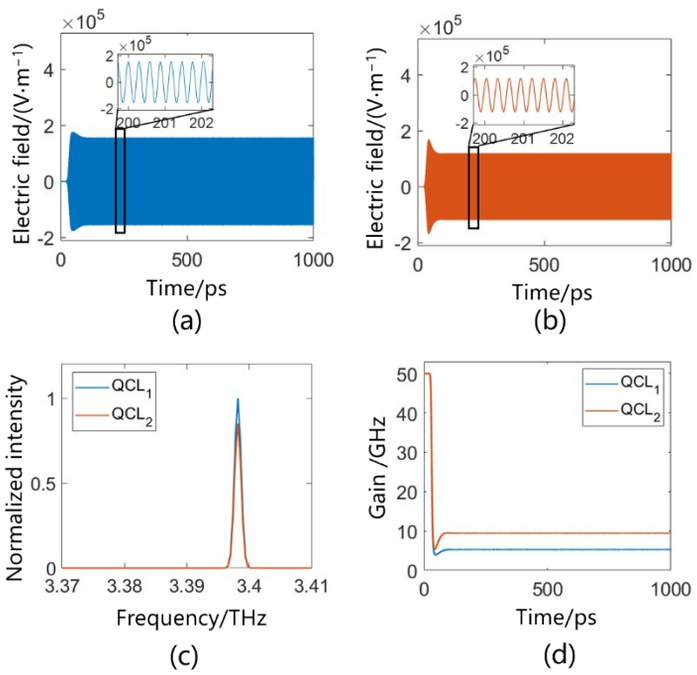

Fig. 7 Simulations of the lasing dynamics of Array A based on the nonlinear TDFEM under the condition $G_{0,1} = G_{0,2} = 50$ GHz: (a, b) Temporal evolution of $E_{z,1}$ and $E_{z,2}$, respectively, with enlarged views shown in the insets. (c) Steady-state spectra of $E_{z,1}$ and $E_{z,2}$. (d) Temporal evolution of the gains. In all panels, the blue and red curves are associated with QCL_1 and QCL_2, respectively.
图7 在G0,1=G0,2= 50 GHz的条件下,阵列A基于TDFEM的激射过程的模拟:(a, b) 分别Ez,1和Ez,2的时域演化,插图为局部放大;(c) Ez,1和Ez,2的稳态频谱;(d) 增益的时域演化。在所有的图中,蓝色和红色曲线分别对应QCL1和QCL2有关的物理量。

time-independent electric field amplitudes and gains in steady-state. In contrast, QCL_2 supports both modes with comparable intensity, leading to strong oscillations in both the electric field amplitudes and gains. The oscillation frequency is equal to the beat frequency between the two lasing modes. Comparison between the results of the nonlinear TCMT model (Figs. 2 and 3) and those of nonlinear TDFEM (Figs. 7 and 8) shows high consistency in terms of field amplitudes, synchronization behaviors, lasing frequencies, and steady-state gains. Notably, the computational time of the former is approximately 1/10000 of that required by the latter.

Following the experimental procedure, we further simulate the frequency tuning and radiation power of Arrays A and B using the nonlinear TDFEM, with the gain tuning parameter d' varying from 0 to 1. To calculate the radiation power, we first evaluated the transient Poynting vectors at a distance approximately two wavelengths above the device, where near-field contributions are negligible. Since the simulations are 2D, the calculated fields correspond to the cross section at $y = 0$. 3D frequency-domain eigenmode analysis shows that the ratio of the surface integral of the Poynting vector over the device surface to the line integral of the Poynting vector along the central line ($y = 0$) is approximately 1.18×10^{-4} m. Using this ratio, the actual 3D radiation power can be estimated from the 2D simulations.

Fig. 9(a) shows the calculated steady-state lasing spectra of Array A for different values of d'. The two sublasers are synchronized and the array remains single-mode throughout the entire tuning process. The lasing frequency continuously redshifts from 3.401 THz to 3.390 THz, in good agreement with the experimentally observed tuning range of 3.407 – 3.397 THz, with a discrepancy of only 9%. The experimentally measured frequencies are slightly higher than the simulated values, which may arise from fabrication tolerances or uncertainties in the refractive-index parameters used in the simulations. Experimentally, the lasing frequency does not vary strictly monotonically with d, whereas the simulated frequency changes monotonically with d'. The primary reason is that the gain of the THz-QCL active region does not vary linearly with the driving current and may even exhibit nonmonotonic behavior. Fig. 9(b) shows the simulated radiation power of Array A for different values of d', and the overall trend agrees with the experimental results shown in Fig. 1(d).

Figs. 9(c) and 9(d) show the steady-state spectra of $E_{z,1}$ and radiation power of Array B as functions of d'. During the tuning process, the array initially operates in high-frequency mode. When $0.5 < d' < 0.7$, both high- and low-frequency modes lase simultaneously, whereas for $d' > 0.7$, the array abruptly switches to the low-frequency mode. The simulated evolution from high-frequency lasing to dual-mode operation and finally to low-frequency lasing is consistent with the experimental observations shown in Fig. 1(e). The main discrepancy is that the experimentally observed dual-mode regime occurs within a narrower current tuning range $0.4 < d' < 0.45$, most likely because the gain is not linearly related to the pump current.

Compared with the experimentally measured radia-

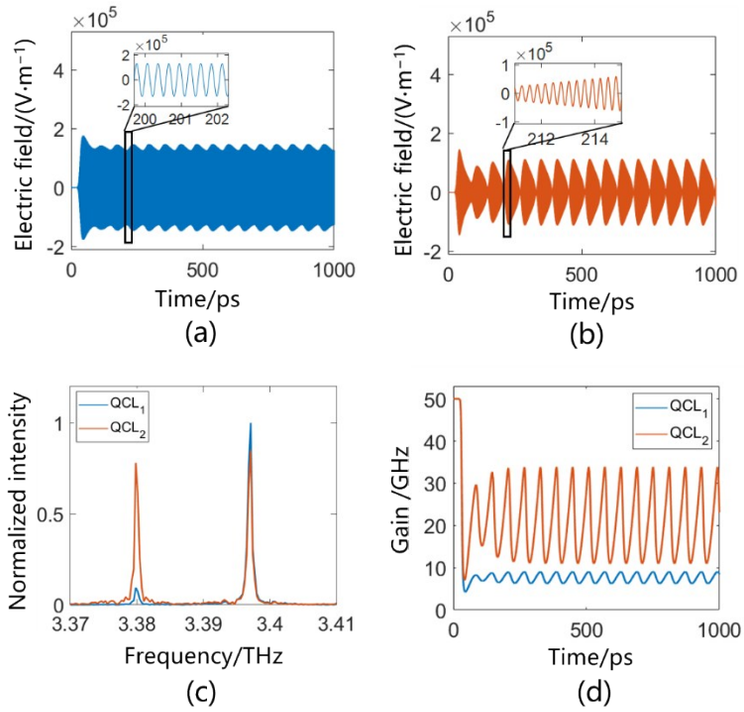

Fig. 8 Simulations of the lasing dynamics of Array B based on the nonlinear TDFEM under the condition $G_{0,1} = G_{0,2} = 50$ GHz: (a, b) Temporal evolution of $E_{z,1}$ and $E_{z,2}$, respectively, with enlarged views shown in the insets. (c) Steady-state spectra of $E_{z,1}$ and $E_{z,2}$. (d) Temporal evolution of the gains. In all panels, the blue and red curves are associated with QCL_1 and QCL_2, respectively.
图8 在G0,1=G0,2= 50 GHz的条件下,阵列B基于非线性TDFEM的激射过程的模拟:(a, b) 分别为Ez,1和Ez,2的时域演化,插图为局部放大;(c) Ez,1和Ez,2的稳态频谱;(d) 增益的时域演化。在所有的图中,蓝色和红色曲线分别对应QCL1和QCL2有关的物理量。

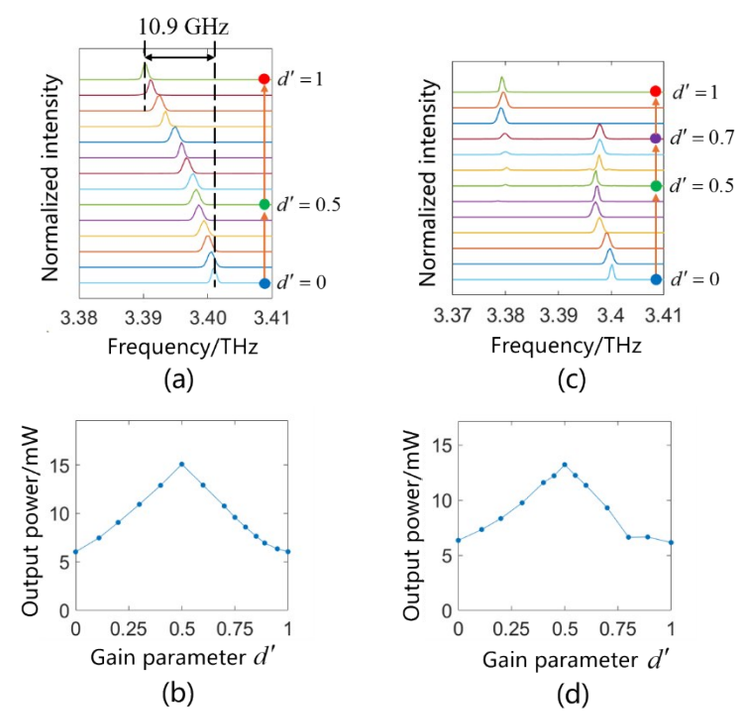

Fig. 9 Simulated tuning characteristics of representative binary THz-QCL arrays based on the nonlinear TDFEM: (a) Lasing spectra and (b) radiation powers of Array A as the gain parameter d' increases from 0 to 1. (c, d) Corresponding results for Array B. In (a) and (c), blue, green, purple, and red dots correspond to $d' = 0$, 0.5, 0.7 and 1, respectively.
图9 基于TDFEM的典型二元THz-QCL阵列调谐特性的模拟结果:(a, b) 阵列A在增益调谐参数d'从0增加到1过程中的(a)激射光谱,以及(b)辐射功率;(c, d) 阵列B对应的结果。图(a)和(c)中,蓝、绿、紫和红点分别对应d'= 0、0.5、0.7和1。

tion power (Figs. 1(d) and 1(f)), the simulated radiation power (Figs. 9(b) and 9(d)) exhibits relatively large discrepancies in both its absolute value and its overall variation with the tuning parameter. Possible reasons are as follows: (1) Use of empirical parameters in the simulations. Several parameters were assigned empirical values, including a waveguide loss of 10 cm^{-1}, a maximum net gain of 40 cm^{-1}, and the real part of refractive index of 3.55, the saturation energy density W_{sat}. (2) The non-monotonic relationship between the pumping current and the material gain. Before the onset of lasing, the gain may decrease with increasing pumping current (equivalently, the effective loss increases)[34], giving rise to the two local minima observed in the experimental output-power curve. (3) Discrepancy between eigenfrequency simulation and time-domain simulation when calculating Poynting vectors ratio. Because 3D time-domain simulations are computationally intensive, the ratio was determined using eigenfrequency simulations with a linear gain model.

Comparison between the results of the nonlinear TCMT model (Fig. 4) and those of nonlinear TDFEM (Fig. 9) shows excellent agreement in the predicted lasing frequencies. However, the nonlinear TCMT model can only calculate the average intracavity energy density, whereas the nonlinear TDFEM can directly calculate the radiation power. Overall, the nonlinear TCMT model provides a highly efficient approach for predicting mode competition and frequency tuning in binary laser arrays, while nonlinear TDFEM enables accurate calculations of lasing frequency, tuning characteristics, and radiation power. The combination of these two models provides a powerful framework for designing laser arrays with a maximized tuning range and optimized radiation power.

5 Conclusion

In summary, we developed a TCMT model incorporating gain saturation to efficiently describe mode competition, frequency tuning, and intracavity energy evolution in binary coupled laser arrays. We further developed a TDFEM including nonlinear gain and gain dispersion, enabling accurate simulations of field dynamics, frequency tuning, and radiation power. Both methods show good agreement with the experimental results.

Compared with conventional frequency-domain eigenvalue analysis, the proposed time-domain approaches can directly describe mode competition and radiation characteristics after lasing onset. The combination of the efficient TCMT model and accurate TDFEM therefore provides a practical framework for designing coupled-cavity laser arrays with optimized tuning range and radiation power.

References

[1] Ge H, Wang S, Guo C, et al. Detection of wheat water distribution using THz images and deep learning[J]. Infrared Physics & Technology, 2025, 151: 106062.

[2] Tu S, Zhang C, Song Z, et al. High-precision identification of dihydrouracil, glycine anhydride, and piperazine using terahertz spectroscopy[J]. Infrared Physics & Technology, 2025, 151: 106066.

[3] Leitenstorfer A, Moskalenko A S, Kampfrath T, et al. The 2023 terahertz science and technology roadmap[J]. Journal of Physics D: Applied Physics, 2023, 56(22): 223001.

[4] Faist J. Quantum Cascade Lasers[M]. Oxford University Press, 2013.

[5] Williams B S. Terahertz quantum-cascade lasers[J]. Nature Photonics, 2007, 1(9): 517-525.

[6] Huang J H, Xu G Y. Photonic and electric control in terahertz quantum cascade lasers: Review[J]. Journal of Infrared and Millimeter Waves, 2022, 41(1): 169-180.
(黄嘉豪, 徐刚毅. 太赫兹量子级联激光器中的光电调控:综述[J]. 红外与毫米波学报)), 2022, 41(1): 169-180

[7] Tan C, Zou T T, Zang S Z, et al. Continuous wave operation of terahertz quantum cascade wire lasers with dual coupled gratings[J]. Journal of Infrared and Millimeter Waves, 2026, 45(2): 294-302.

[8] Scalari G, Faist J. 30 years of the quantum cascade laser[J]. Communications Physics, 2024, 7(1): 394.

[9] Tan C, Yan C F, Zang S Z, et al. Research on low-power consumption, high heat dissipation efficiency terahertz quantum cascade laser[J]. Journal of Infrared and Millimeter Waves, 2025, 44(3): 430-439.
(谭诚, 严川峰, 臧善志, 等. 低功耗、高散热效率太赫兹量子级联激光器的研究[J]. 红外与毫米波学报)), 2025, 44(3): 430-439.

[10] Rahman A, Rahman A K, Rao B. Early detection of skin cancer via terahertz spectral profiling and 3D imaging[J]. Biosensors and Bioelectronics, 2016, 82: 64-70.

[11] Christopher K W, Craig K, Paul G, et al. GUSTO: Gal/Xgal U/LDB Spectroscopic-Stratospheric TeraHertz Observatory[C]//Millimeter, Submillimeter, and Far-Infrared Detectors and Instrumentation for Astronomy XI. 2018.

[12] Fitzgerald A J, Wallace V P, Pye R, et al. Terahertz imaging of breast cancer, a feasibility study[C]//Infrared and Millimeter Waves, Conference Digest of the 2004 Joint 29th International Conference on 2004 and 12th International Conference on Terahertz Electronics, 2004. 2004: 823-824.

[13] Vitiello M S, Tredicucci A. Tunable Emission in THz Quantum Cascade Lasers[J]. IEEE Transactions on Terahertz Science and Technology, 2011, 1(1): 76-84.

[14] Hempel M, Röben B, Schrottke L, et al. Fast continuous tuning of terahertz quantum-cascade lasers by rear-facet illumination[J]. Applied Physics Letters, 2016, 108(19): 191106.

[15] Qin Q, Williams B S, Kumar S, et al. Tuning a terahertz wire laser[J]. Nature Photonics, 2009, 3(12): 732-737.

[16] Han N, De Geofroy A, Burghoff D P, et al. Broadband all-electronically tunable MEMS terahertz quantum cascade lasers[J]. Optics Letters, 2014, 39(12): 3480.

[17] Lee A W M, Williams B S, Kumar S, et al. Tunable terahertz quantum cascade lasers with external gratings[J]. Optics Letters, 2010, 35(7): 910.

[18] Castellano F, Bianchi V, Li L, et al. Tuning a microcavity-coupled terahertz laser[J]. Applied Physics Letters, 2015, 107(26): 261108.

[19] Curwen C A, Reno J L, Williams B S. Broadband continuous single-mode tuning of a short-cavity quantum-cascade VECSEL[J]. Nature Photonics, 2019, 13(12): 855-859.

[20] Kundu I, Dean P, Valavanis A, et al. Continuous Frequency Tuning with near Constant Output Power in Coupled Y-Branched Terahertz Quantum Cascade Lasers with Photonic Lattice[J]. ACS Photonics, 2018, 5(7): 2912-2920.

[21] Kundu I, Freeman J R, Dean P, et al. Wideband Electrically Con-

trolled Vernier Frequency Tunable Terahertz Quantum Cascade Laser[J]. ACS Photonics, 2020, 7(3): 765-773.
[22] Khalatpour A, Reno J L, Hu Q. Phase-locked photonic wire lasers by π coupling[J]. Nature Photonics, 2019, 13.
[23] Yan C, Tan C, Wang K, et al. Broadband Continuous Frequency Tuning in Non-Hermitian Laser Arrays Enabled by Mode-Switching Boundary Topology[J]. arXiv preprint, 2026, https://doi.org/10.48550/arXiv.2602.06438.
[24] Amanti M I, Scalari G, Terazzi R, et al. Bound-to-continuum terahertz quantum cascade laser with a single-quantum-well phonon extraction/injection stage[J]. New Journal of Physics, 2009, 11(12): 125022.
[25] Wang K, Bai H, Yu C, et al. Independent Control of Mode Selection and Power Extraction in Terahertz Semiconductor Lasers[J]. ACS Photonics, 2022, 9(6): 1973-1983.
[26] Bacon D R, Freeman J R, Mohandas R A, et al. Gain recovery time in a terahertz quantum cascade laser[J]. Applied Physics Letters, 2016, 108(8): 081104.
[27] Tredicce J R, Arecchi F T, Lippi G L, et al. Instabilities in lasers with an injected signal[J]. Journal of the Optical Society of America B, 1985, 2(1): 173.
[28] Liu J M. Photonic Devices[M]. New York: Cambridge University Press, 2005.
[29] Zhu H, Zhu H, Yu C, et al. Modeling and improving the output power of terahertz master-oscillator power-amplifier quantum cascade lasers[J]. Optics Express, 2020, 28(16): 23239.
[30] Hassan A U, Hodaei H, Miri M A, et al. Nonlinear reversal of the PT -symmetric phase transition in a system of coupled semiconductor microring resonators[J]. Physical Review A, 2015, 92(6): 063807.
[31] Christopoulos T, Tsilipakos O, Kriezis E E. Temporal coupled-mode theory in nonlinear resonant photonics: From basic principles to contemporary systems with 2D materials, dispersion, loss, and gain[J]. Journal of Applied Physics, 2024, 136(1): 011101.
[32] Haus H A, Huang W. Coupled-mode theory[J]. Proceedings of the IEEE, 1991, 79(10): 1505-1518.
[33] Ding J, Belykh I, Marandi A, et al. Dispersive versus Dissipative Coupling for Frequency Synchronization in Lasers[J]. Physical Review Applied, 2019, 12(5): 054039.
[34] Burghoff D, Kao T Y, Ban D, et al. A terahertz pulse emitter monolithically integrated with a quantum cascade laser[J]. Applied Physics Letters, 2011, 98(6): 061112.
[35] Jackson J D. Classical Electrodynamics[M]. Wiley, 2012.

二元太赫兹量子级联激光器阵列频率调谐与辐射功率的建模

高山海[1,2]，王 凯[1*]，谭 诚[1,2]，甘良华[1]，房玉龙[3*]，张月蘅[4]，徐刚毅[1]
（1. 中国科学院上海技术物理研究所，红外探测全国重点实验室，上海 200083；
2. 中国科学院大学，北京 100049；
3. 河北半导体研究所，河北 石家庄 050051；
4. 上海交通大学，物理与天文学院，上海 200083）

摘要：发展了两种互补的方法以模拟二元太赫兹量子级联激光器(THz-QCL)阵列中的模式竞争、频率调谐和辐射功率。第一种方法基于包含非线性增益的时域耦合模理论模型，能够高效地模拟激射后腔内电场振幅和增益的演化。该方法复现了实验观测到的模式竞争和频率调谐行为，并预测了最大连续调谐范围。第二种方法基于包含非线性增益和增益频率色散的时域有限元法。该方法明确包含了具体的谐振腔结构，因此除了能模拟模式竞争和频率调谐外，还能准确模拟辐射功率。模拟结果与实验测量吻合良好，频率调谐范围误差为9%，辐射功率误差约为50%。两种方法的结合使用为优化二元耦合激光器阵列的频率调谐范围和辐射功率提供了有效的框架。此外，这两种方法不仅适用于二元THz-QCL阵列，还可推广至增益响应延迟可忽略的一般Class-A耦合激光器。

关 键 词：太赫兹量子级联激光器；非线性增益；模式竞争；频率调谐；辐射功率；时域耦合模理论；时域有限元方法

中图分类号：O43 **文献标识码**：A